Monitoring density and temperature in C/C composites elaborated by CVI with induction heating

David Leutard, Gerard L. Vignoles, Franck Lamouroux, Bruno Bernard

Manuscript submitted to *J. Mater. Synth and Proc.*

MONITORING DENSITY AND TEMPERATURE IN C/C COMPOSITES PROCESSING BY CVI WITH INDUCTION HEATING

David Leutard[1], Gérard L. Vignoles[2,3], Franck Lamouroux[1] and Bruno Bernard[1]

[1]SNECMA Rocket Engine Division, Les Cinq Chemins, Le Haillan, F33165 ST-MEDARD-en-JALLES, France

[2]Laboratoire des Composites ThermoStructuraux (UMR 5801 CNRS-SNECMA-CEA-UB1) , 3, Allée La Boëtie, Université Bordeaux 1, F33600 PESSAC, France. Fax : (00 33) 5 56 84 12 25, e-mail : vinhola@lcts.u-bordeaux.fr

[3]to whom correspondence should be addressed

Suggested running title : Monitoring Density and Temperature in RF-CVI C/C processing.

Abstract. Carbon/Carbon composites are processed by Chemical Vapor Infiltration (CVI) with radio-frequency inductive heating, which leads to inside-out temperature gradients, suitable for the production of homogeneously densified pieces if properly controlled throughout the whole processing. We present here a 2D axisymmetrical case where a comprehensive numerical model is tested against experimental runs. The numerical thermal model takes into account induction heating, radiative, conductive, and convective effects, intermediate regime diffusion and densification reactions in the pores, and the evolution of the porous medium. The results are the time evolution of the temperature, concentration and composite material density field, as well as the input power necessary to ensure a given maximal temperature in the preform. Experimental data are measurements of the temperature and density fields at various infiltration stages. Comparison between experience and simulation, yielding an useful agreement, allows to show that porosity gets trapped inside the preform as densification proceeds, because of the progressive lowering of the temperature gradient steepness. The discrepancies between computations and experimental data rely on the only approximate knowledge of some quantities, principally the reaction kinetics, which are currently under investigation.

Key words. C/C composites, processing, numerical modeling.

1 INTRODUCTION

Carbon/carbon composite materials are more and more frequently used in high-temperature applications such as rocket nozzle heat shields, airplane brakes, and furnace components. For a high thermal and mechanical quality, CVI-processed pieces are preferred. CVI stands for Chemical Vapor Infiltration, a process derived from CVD (Chemical Vapor Deposition) , in which a preform made of carbon fibers is densified by a pyrocarbon deposit originated in the cracking of gaseous pyrocarbons, usually at high temperatures (*ca.* 1000-1300 K) and low to atmospheric pressures. This process allows the fabrication of complex pieces without damaging the carbon fibers and results in excellent mechanical and thermal properties.

The classical implementations of CVI are the isothermal-isobaric process (I-CVI) [1, 2], and the forced CVI (F-CVI) process [3–8]. The latter method has been improved by the application of a thermal gradient from the gas-outlet side to the gas-inlet side, thus allowing the pores to be filled from their remote extremity first.

Similarly to this, but without forcing the gases inside the preform, are a variety of nearly isobaric, thermal-gradient CVI (TG-CVI) techniques. The use of a central susceptor bringing heat to the inner surface of a crown-shaped preform has been investigated by several authors [9–11].

Some preliminary experimental studies have been performed on microwave heating of Nicalon ®fiber preforms [12, 13] associated to SiC/Si deposition ; the results encouraged other teams to further investigate in the direction of volume-heating techniques.

A newer variant is the CVI with direct radio-frequency inductive heating of the preform (RF-CVI) [14, 15]. In this technique, inside-out temperature gradients appear in the preform irrespective of its shape, in contrast to F-CVI. Such thermal gradients are appropriate to obtain a complete densification of the material, since the pores begin to be filled at their most remote part first.

Available experimental reports on the thermal-gradient CVI process of carbon-carbon composites are mainly due to Golecki and co-workers [16–20]. They have used C_5H_{10} as a gaseous precursor, a radio-frequency range of 4.9-8.6 kHz, which lead to temperatures in the range of 1000 to 1450 K ; the preforms displayed an inside-out initial temperature field, which eventually turned outside-in in the last third of the densification run (see fig. 6 of [17]). The preform density has been determined after 1/4 and 1/2 of the total processing time, with well-marked

inside-out density gradients. The final density field is not displayed.

A variant featuring temperature and pressure pulsing (TP-CVI) has also been studied experimentally [21], with excellent results for pyrocarbon and SiC infiltration.

Theoretical investigations of thermal-gradient CVI went in various directions. They are either 1D or 2D, and account for heat gains by various ways : imposed boundary temperatures, constant power distributions, or preliminary solving of Maxwell's equations, while heat losses are represented by convective and/or radiative heat exchange boundary conditions. Various chemical systems have been also used. Table 1 is an attempt to compile several of these references.

These studies have first shown that inside-out temperature gradients could potentially favor a complete densification, and that the total processing time may be well diminished with respect to I-CVI. However, it is shown that minimal temperature gradients are necessary to ensure the desired situation. In refs. [14, 22, 23] computations are shown where the correct situation is obtained at the beginning of densification, and the outside-in situation later appears.

However, no direct confrontation between numerical simulations and experimental data has been reported, to the authors' knowledge. The present study is an attempt to provide such a confrontation between experimental results and a comprehensive numerical model containing all features described in [14], plus gas convection effects and a more accurate description of radiative heat transfer .

2 EXPERIMENTAL SETUP

A cylindrical reactor is heated by induction coils made of copper tubes inside which a coolant fluid flows. A crown-shaped preform is held approximately at half-height inside the reactor. Two refractory bricks are located above and below the preform, in order to provide it with a partial heat insulation. The gases enter the chamber from below, and exit from above. The apparatus heating is driven with a temperature regulation, that is, the RF coil electrical power is regularly updated so that the temperature at the center of the preform (as measured with a thermocouple) is held constant. The whole setup scheme is shown at fig. 1.

The parameters describing the reactor are summarized at table 2. The gas flow rate is cho-

sen as very high, in contrast to typical I-CVI conditions. The reason for this is that it is tried to obtain a convective freshening of the preform's inner surface - indeed, this region undergoes relatively small radiative heat losses, and the inside-out temperature gradient in this region would be too low to ensure proper densification.

Two different kinds of gas inlet compositions have been chosen : first, pure nitrogen in order to check out the thermal computations without any side-effect owed to densification, and second, methane. In the latter case, to take into account a partial decomposition of the gas leading to hydrogen production, an arbitrary amount of 25% of H_2 has been chosen for the thermal computations. Indeed, hydrogen has thermal properties that differ strongly from any other gas, and this fact led us to take it into account.

3 EXPERIMENTAL RESULTS

The preform temperature field has been monitored by a set of 9 thermocouples evenly spaced in a radial section, at three axial positions and three radial positions. The temperature dataset is then interpolated linearly to give approximate representations of the whole temperature field. Also, the density has been monitored in the preform at various densification stages by a destructive method. After stopping the infiltration, three radial slices are extracted from the preform, then split into 9 drill cores for which density is individually determined by classical weight and volume measurements. The results are then interpolated as for temperature in order to visualize the density field. Fig. 2 shows the disposition of the thermocouples and the position of the drill cores in the preform.

Fig.3 shows the recorded temperature fields using either N_2 or CH_4. It is clearly apparent that the difference between both fields lies essentially in the lower left corner of the preform section. More precisely, the cooling owed to the gas stream is much more important when CH_4 is used. This is due to the different thermal properties of these gases : CH_4 is more conductive than N_2, and becomes even more if it is partially decomposed into H_2.

Figs. 4 and 5 show the respective time evolutions of the temperature and density fields, as determined experimentally. Coherently with previous results of the literature, it is seen that, even if the desired inside-out density gradient appears at the early stages of densification, a

central minimum eventually shows up after some time. This is due to the fact that the denser the preform, the higher its heat conductivity. After a while, the temperature gradients are not steep enough to counteract the natural tendency that exists in I-CVI, and a moderate outside-in gradient is seen at 80% total processing time.

4 NUMERICAL MODEL

The modelling strategy in this study is in many points comparable to that previously reported in [14]. We refer to this article for a complete description, indicating only the differences which have been introduced here. All computations were performed with a general-purpose finite-element PDE solver allowing to chain together different computations [24].

4.1 Heat transfer simulation

The first modelling step is to compute the electromagnetic field by a solution of Maxwell's equations, under the potential-vector formulation :

$$\begin{cases} \nabla \times (\nu_r \nabla \times \mathbf{A}) - \nabla (\nu_p \nabla \cdot \mathbf{A}) + \mu_0 \sigma_\theta (\omega \mathbf{A} - \nabla V) = \mathbf{J}_s \\ \nabla \cdot \left(\sigma_\theta \left(\frac{\partial \mathbf{A}}{\partial t} + \nabla V \right) \right) = 0 \end{cases} \tag{1}$$

, where the unknowns are the vector potential $\mathbf{A}$ such that the magnetic field $\mathbf{B}$ be equal to $\nabla \times \mathbf{A}$, and the (scalar) electric potential V. The material parameters are the relative magnetic reluctivity $\nu_r = 1/\mu_r$ and the orthoradial component σ_θ of the electric conductivity.

The second term in the left-hand side is a numerical penalization term, with a non-physical parameter ν_p, which removes the singularity of the equation. The injected power is directly written under the form of a source term $\mathbf{J}_s$, whose intensity is determined from the knowledge of the input current intensity I and the conduction skin depth in the coils $e = (\pi \sigma \omega \mu_0)^{-1}$. All quantities are complex, since we are dealing with oscillatory currents.

The technique of "infinite elements" is used to represent the boundary conditions at infinite distance.

As a result of the computations, the amount of power dissipated by Joule effect inside the

preform is computed :

$$Q_{th} = (2\sigma_\theta)^{-1} \mathbf{J}\overline{\mathbf{J}} \tag{2}$$

where the induced electrical current density is :

$$\mathbf{J} = \nabla \times \left(\nu_r \mu_0^{-1} \nabla \mathbf{A}\right) \tag{3}$$

The dissipated power is then treated as a volumic heat energy source for the subsequent thermal computation.

The heat equation that is considered here takes into account conduction and convection, as well as the previously mentioned heat source, and covers both the preform and the surrounding gas-phase :

$$\rho C_p \frac{\partial T}{\partial t} + \rho C_p \mathbf{v} \cdot \nabla T + \nabla \cdot \left(-\underline{\underline{\lambda}} \nabla T\right) = Q_{th} \tag{4}$$

In the preform, the conductivity is treated as a tensor in the porous medium to represent orthotropic behavior, and $\mathbf{v}$ is set to zero. The temperature in the porous medium is treated as equal in the fluid and solid phases, since they have a very important heat exchange interface. In the gas-phase, the conductivity is scalar, and the source term is set to zero. Heat sources or sinks related to chemical reactions are neglected since the enthalpy changes in the case of hydrocarbon pyrolysis are not very large. The velocity field $\mathbf{v}$ in the gas is obtained by a resolution of the continuity and Navier-Stokes equations (total mass and momentum balances) :

$$\frac{\partial (\rho \mathbf{v})}{\partial t} + \nabla \cdot (\rho \mathbf{v} \otimes \mathbf{v}) + \nabla . \underline{\underline{\tau}} - \nabla \cdot \left(P \underline{\underline{I}}\right) = \rho \mathbf{g} \tag{5}$$

$$\underline{\underline{\tau}} = -\mu \left(\nabla \mathbf{v} + {}^t \nabla \mathbf{v}\right) + \frac{2}{3} \nabla \cdot \mathbf{v} \tag{6}$$

$$\frac{\partial \rho}{\partial t} + \nabla \cdot (\rho \mathbf{v}) = 0 \tag{7}$$

In the porous medium, velocity is considered as zero, since it is of negligible importance.

Radiation is described with a multireflecting radiating cavity formalism with a full 3D form-factor computation, considering the reactor as a quasi-closed cavity. The radiative exchange between the walls of the cavity are represented by the following boundary conditions :

$$\left(-\underline{\underline{\lambda}} \nabla T\right) \cdot \mathbf{n} = \phi_r \tag{8}$$

where the radiative fluxes are obtained by the following relations for discretized surface elements :

$$[A]\, \phi_r = [B]\, T^4 \tag{9}$$

$$A_{ij} = e_j^{-1} \left(\delta_{ij} - (1 - e_j) F_{ij} \right) \tag{10}$$

$$B_{ij} = \sigma_s \left(\delta_{ij} - F_{ij} \right) \tag{11}$$

$$F_{ij} = \frac{1}{S_i} \int_{S_i} \int_{S_j} \frac{\cos\theta_i \cos\theta_j dS_i dS_j}{r_{ij}^2} \tag{12}$$

in which

- σ_s is Stefan's constant $(5,67.10^{-8}\ W.m^{-2}.K^{-1})$
- δ_{ij} is the Kronecker symbol ;
- e_i is the emissivity of the i^{th} surface element ;
- S_i is the area of the i^{th} surface element (m^2).
- $\mathbf{r}_{ij}$ is a vector linking the centers of the i^{th} and j^{th} elements.
- θ_i is the angle between the normal to the i^{th} element and $\mathbf{r}_{ij}$
- F_{ij} is the form-factor of element i for element j. It gives the fraction of the flux emitted by i that is received by j.

Incorporating gas convection and multireflection radiation allows to represent in a much more realistic way the distribution of the heat fluxes that are lost by the preform, than in the previous modeling works. This was an important necessity in our case because of the chosen experimental setup, for which the temperature field is extrememly sensitive to both radiative and convective losses at the preform surfaces.

The choice of a model for thermal conductivity is also critical for the accuracy of the temperature field. We have taken here into account the anisotropy of the preform, and the fact that conductivity of non-graphite carbons increases with temperature [25, 26], which is indeed the case for both carbon fibers and infiltrated pyrocarbons. All estimated preform properties are listed in table 3.

Thermal regulation is implemented in the simulation through an iterative algorithm. A first computation yields a temperature field whose maximal value inside the preform is compared to the prescribed temperature ; the power is increased or decreased if both temperatures differ by more than 10 K.

4.2 Densification simulation

The model that has been used for densification is relatively simple and relies on a quasi-steady-state assumption, that is, it has been considered that the porous medium properties such as density evolve slowly with respect to the transient time scale of gas transport phenomena. A steady-state diffusion equation is first solved to obtain the repartition of the precursor gases in the preform ; then the densification rate is tabulated and reused for the evaluation of the porosity evolution some time later.

The transport and reaction of only one species has been solved ; no convection (Darcy) effects have been taken into account since they are lower by more than two orders of magnitude than diffusion effects ; a first-order deposition kinetic law has been taken. This is summarized in the following equation :

$$\nabla \cdot (-D_{eff} \nabla C) = -\sigma_v k C \tag{13}$$

The most important structural parameters are then the effective diffusivity D_{eff} and internal surface area σ_v, the latter determining the importance of the heterogeneous reaction. The laws that have been chosen for these quantities are described in table 3. The results of Monte-Carlo computations for overlapping cylinders randomly disposed in 2 dimensions [27] have been used to model the radial and axial effective gas diffusivities. The various laws have been slightly altered to take into account a percolation porosity of 0.07. Classical models for the gas properties (density, viscosity, thermal conductivity, heat capacity, free gas pair diffusivity) [28] have been otherwise employed. Once eq. (13) has been solved, the mass sink term $\sigma_v k C$ is reused in the following ordinary differential equation :

$$-\frac{\partial \epsilon}{\partial t} = v_s \sigma_v k C \tag{14}$$

The whole numerical procedure is sketched in fig. 6.

5 NUMERICAL RESULTS AND DISCUSSION

5.1 Momentum transfer

The structure of the reactor is such the flow patterns are very difficult to compute. A preliminary determination of the local Re and Ra dimensionless numbers in various parts of the reactor are summarized in table 4. According to universal correlations [29], they lead to predict flow regimes that are of two kinds :

- The preform inner hole and the outlet zone in which the flow is forced and is close to turbulence;
- The other parts of the reactor for which the flow is much more laminar and mainly of natural convection nature.

Accordingly, it has been necessary to compute the velocities with a transient form of the Navier-Stokes equations, and wait for a permanent regime to settle itself (approximately in 40 real-time seconds).

The flow pattern is sketched in fig. 7. It is apparent that the gases mainly propagate through the inner hole of the preform up to the outlet, leading to the desired convective refreshment of the inner hole surface. Some convection loops, due to either forced or natural convection circulate above the preform. A moderate downwards stream is present around the outer radius of the preform.

5.2 Initial temperature fields

The temperature fields that have been computed in both cases (N_2 and CH_4/H_2) have been compared to the experimental data, as reported in figs. 8 and 9. The agreement is generally excellent. In the first case, the relative discrepancy between calculations and measurements is less than 5% over more than 70% of the preform section area. In the case of CH_4/H_2, the agreement is lesser : indeed, the gas mixture that has been used for the computations is only

a rough approximation of the true gas composition, and its thermal properties seem to have been underestimated.

In order to quantify the impact of gas convection on the thermal field, another numerical calculation has been performed without convection , and the difference between the temperature fields is displayed in fig. 10 : a clear zone of influence appears in the inner part of the section, for which there is a temperature lowering of roughly 50 K using N_2 and 100 K using methane. Even though this is somewhat lower than the experimental values, the correct tendencies are well described.

The radiative fluxes are displayed in fig. 11. As expected, they are much lower at the inner face of the preform than at the outer face, and this is compensated here by the convective loss. The upper and lower faces are partially insulated by the refractory bricks : this helps to force the isotherms to be more perpendicular to the radial direction. At the center of the outer surface of the preform, it has been evaluated that the radiative heat loss is 96% of the total, while it is only 81% at the inner face.

5.3 Density and temperature evolution

The evolution of the density and temperature fields, as computed with our model, is shown in figures 12 and13. On the former, it is clearly apparent that the main feature of the experimental behavior is qualitatively reproduced : the density field, at first with the desired inside-out gradient, begins to display a central minimum at a unit dimensionless time, for which the maximal density is still 1.45 $g.cm^{-3}$. Also, the effect of convection on the interior lower corner of the preform section is reproduced, though with a lesser extent, since it becomes perceptible only at the latest stages of densification.

There are some differences between numerical and experimental densification results.

First, the time-scale for the numerical densification is larger : such a discrepancy is not surprising, taking into account the fact that it has not been tried to optimize the deposition rate law. The experimental and computed average density and temperature evolutions would be very similar if the dimensionless time were rescaled by a factor of 1/5 for the numerical densification.

Second, the inner depleted zone is much larger in the model than in the experience. Various

reasons are plausible for that :

- An overestimation of the reaction/diffusion ratio, either because of an overestimation of the surface area or because of an underestimation of the effective diffusion coefficient ;
- An under-estimation of the chemical reaction activation energy, since it is the key parameter for the importance of the desired inside-out density gradient.

Third, the computed temperature average displayed at figure 13 tends to a lower limit than the experimental one. This comes probably from an underestimation of the thermal diffusivity in the preform, especially when it gets densified. One could guess from those results that the thermal conductivity of the carbon matrix is higher than for the fibers.

The evolution of various other quantities has been followed in the preform in order to track which one exhibits first a gradient non-monotonicity. It appears that the densification rate $-\partial\epsilon/\partial t = kC$ displays an M-shaped radial profile at a dimensionless time of 0.8, in advance with respect to the density. This is to be expected from the antagonist rôle of the rate constant, which depends on the temperature and the internal surface, and the concentration which tends to be less active at the center because of diffusional limitations. Once the preform center is partially densified, the conductivity increase induces a thermal gradient decrease, which eventually ceases to counteract the concentration depletion. The higher the activation energy, the later this phenomenon occurs.

6 CONCLUSION

A coherent set of numerical predictions and experimental data has been produced for the RF-CVI processing of carbon/carbon composites, in the case of a crown-shaped piece. Both procedures use a thermal regulation loop maintaining a constant temperature at the preform center, and a strong convective refreshment of the inner section by the inlet gases, which compensates the lower importance of radiative thermal losses. Temperature and density have been monitored, showing that the final stages of RF-CVI eventually lead to a situation closer to I-CVI, which is an adverse effect for the C/C composite quality. Both approaches display a final M-shaped radial density distribution, rather equilibrated from the inner to the outer radius. The agreement is excellent on a thermal point of view, and only qualitative for the density

evolution, probably due to a lack of precise knowledge of thermal, electrical, geometrical, and transport properties in the preform during densification. Future work will be devoted to the determination of such properties, to enhance the physico-chemical precision of the modeling suite, and to use it in order to optimize the process parameters.

Acknowledgements

The authors are indebted to SNECMA and Conseil Régional d'Aquitaine for their financial support in software and hardware equipment.

References

[1] F. Christin, R. Naslain, and C. Bernard, in *Proc. 7th International Conference on CVD*, T. O. Sedgwick and H. Lydtin, eds. (The Electrochemical Society Proceedings Series, Pennington, NJ, 1979), pp. 499–514.

[2] R. Naslain, J. Y. Rossignol, P. Hagenmuller, F. Christin, L. Héraud, and J. J. Choury, *Rev. de Chim. Min.*, **18**, 544–551 (1981).

[3] D. P. Stinton, T. M. Besmann, W. M. Matlin, T. L. Starr, and W. A. Curtain, in *Ceramic Matrix Composites - Advanced High-Temperature Structural Materials*, R. A. Lowden, M. K. Ferber, J. R. Hellmann, K. K. Chawla, and S. G. DiPietro, eds. (Materials Research Society, Pittsburgh, PA, 1995), pp. 317–324.

[4] D. P. Stinton, R. A. Lowden, and T. M. Besmann, in *Chemical Vapor Deposition of Refractory Metals and Ceramics II*, T. M. Besmann, B. M. Gallois, and J. W. Warren, eds. (Materials Research Society, Pittsburgh, PA, 1992), pp. 233–237.

[5] M. Jones and T. L. Starr, in *Proc 19th Annual Conference on Composites, Advanced Ceramics, Materials, and Structures - B*, G. N. Pfendt, ed. (The American Ceramic Society, Westerville, OH, 1995), pp. 829–836.

[6] T. M. Besmann and J. C. McLaughlin, in *Proceedings of the 18th Annual conference on Composites and Advanced Materials - B*, K. V. Logan, ed. (The American Ceramic Society, Westerville, OH, 1994), pp. 897–907.

[7] T. L. Starr and A. W. Smith, in *Chemical Vapor Deposition of Refractory Metals and Ceramics*, T. M. Besmann and B. M. Gallois, eds. (Materials Research Society, Pittsburgh, PA, 1990), pp. 55–60.

[8] N. H. Tai, T. W. Chou, and C. C. M. Ma, *J. Amer. Ceram. Soc.* **77**, 849–872 (1994).

[9] R. R. Melkote and K. F. Jensen, in *Chemical Vapor Deposition of Refractory Metals and Ceramics*, T. M. Besmann and B. M. Gallois, eds. (Materials Research Society,Pittsburgh, PA, 1990) pp. 67–72.

[10] D. J. Skamser, H. M. Jennings, and D. L. Johnson, *J. Mater. Res.* **12**, 724–737 (1997).

[11] M. Kawase, Y. Ikuta, T. Tago, T. Masuda, and K. Hashimoto, *Chem. Eng. Sci.* **49**, 4861–4870 (1994).

[12] D. J. Devlin, R. S. Barbero, and K. N. Siebein, in *Chemical Vapor Deposition XIII*, M. D. Allendorf, McD. Robinson, and R. K. Ulrich, eds. (The Electrochemical Society, Pennington, NJ, 1996), pp. 571–579.

[13] D. J. Devlin, R. P. Currier, R. S. Barbero, and B. F. Espinoza, in *Chemical Vapor Deposition of Refractory Metals and Ceramics II*, T. M. Besmann, B. M. Gallois, and J. W. Warren, eds. (Materials Research Society, Pittsburgh, PA, 1992), pp. 245–250.

[14] V. Midha and D. J. Economou, *J. Electrochem. Soc.* **144**, 4062–4071 (1997).

[15] V. Midha and D. J. Economou, *J. Electrochem. Soc.* **145**, 4062–4071 (1998).

[16] I. Golecki, R. C. Morris, and D. Narasimhan, in *Chemical Vapor Deposition XIII*, M. D. Allendorf, McD. Robinson, and R. K. Ulrich, eds. (The Electrochemical Society, Pennington, NJ, 1996), pp. 547–551.

[17] I. Golecki, R. C. Morris, and D. Narasimhan, in *Proc 19th Annual Conference on Composites, Advanced Ceramics, Materials, and Structures - A*, G. N. Pfendt, ed. (The American Ceramic Society, Westerville, OH, 1995), pp. 315–322.

[18] I. Golecki, R. C. Morris, and D. Narasimhan, *Appl. Phys. Lett.* **66**, 2334–2336 (1995).

[19] I. Golecki, in *Proc. 21st Annual Conference and Exposition on Composites, Advanced Ceramics, Materials and Structures - B*, J. P. Singh, ed. (The American Ceramic Society, Westerville, OH, 1997), pp. 721–730.

[20] I. Golecki, R. C. Morris, D. Narasimhan, and N. Clements, in *Advanced Synthesis and Processing of Composites and Advanced Ceramics II*, K. V. Logan, Z. A. Munir, and R. M. Spriggs, eds. (The American ceramic Society,Westerville, OH, 1996), pp. 135–142.

[21] S. Bertrand, J.-F. Lavaud, R. El-Hadi, G. L. Vignoles, and R. Pailler, *J. Eur. Ceram. Soc.* **18**, 857–870 (1998).

[22] D. Gupta and J. W. Evans, *J. Mat. Res.* **6**, 810–828 (1991).

[23] J. I. Morell, D. J. Economou, and N. R. Amundson, *J. Electrochem. Soc.* **139**, 328–342 (1992).

[24] Flux-Expert finite element software package, distributed by Simulog, France.

[25] A. Herpin, J. Rappeneau, M. Yvars, and R. Setton, *Conductibilité Thermique du graphite et des carbones* (Masson, Paris, 1965).

[26] R. W. Powell and F. M. Schoffield, *Proc. Phys. Soc. London* **51**, 153–167 (1939).

[27] M. M. Tomadakis and S. V. Sotirchos, *J. Chem. Phys.* **98**, 616–626 (1993).

[28] R. C. Reid, J. M. Prausnitz, and B. E. Poling, *The properties of gases and liquids* (McGraw Hill, New York, 1987).

[29] B. Métais and E. R. G. Eckert, *J. Heat Transf.* **86**, 295–302 (1964).

[30] M. K. King, *J. Mat. Res.* **9**, 74–90 (1994).

[31] J. I. Morell, D. J. Economou, and N. R. Amundson, *J. Mater. Res.* **7**, 2447–2457 (1992).

[32] J. Y. Ofori and S. V. Sotirchos, *J. Mater. Res.* **11**, 2541–2555 (1996).

[33] J. I. Morell, D. J. Economou, and N. R. Amundson, *J. Mater. Res.*, **8**, 1057–1067 (1993).

[34] D. Evans and J. W. Evans, *J. Amer. Ceram. Soc.* **76**, 1924–1932 (1993).

Figure Captions.

- Figure 1: Scheme of the experimental apparatus.
- Figure 2: Preform analysis : position of the thermocouples (left) and position of the drill cores for density determination (right).
- Figure 3: Temperature fields in the preform as obtained by interpolation from measured data. Left : with N_2 as the surrounding gas, right : with CH_4 as the surrounding gas, at initial densification stage.
- Figure 4: Average temperature and temperature field evolution in the preform as obtained by interpolation from measured data.
- Figure 5: Average density and density field evolution in the preform as obtained by interpolation from measured data.
- Figure 6: Sketch of the numerical procedure.
- Figure 7: Velocity and temperature fields in the central part of the reactor.The velocities in the innermost part are not displayed for being too high.
- Figure 8: Temperature field in the preform with N_2 as the surrounding gas. Left: computed temperatures, right: relative differences (%) with experimental values.
- Figure 9: Temperature field in the preform with CH_4 as the surrounding gas. Left: computed temperatures, right: relative differences (%) with experimental values.
- Figure 10: Evaluation of the influence of gas convection : temperature difference maps for computations carried with and without convection. Left : N_2 case, right : CH_4 case.
- Figure 11: Radiative heat losses from the preform. a) : on all faces, b) : at the inner and outer faces.
- Figure 12: Computed density evolution : average and maximal density compared to measured values, and density field snapshots at different stages.
- Figure 13: Computed average temperature evolution compared to measured values.

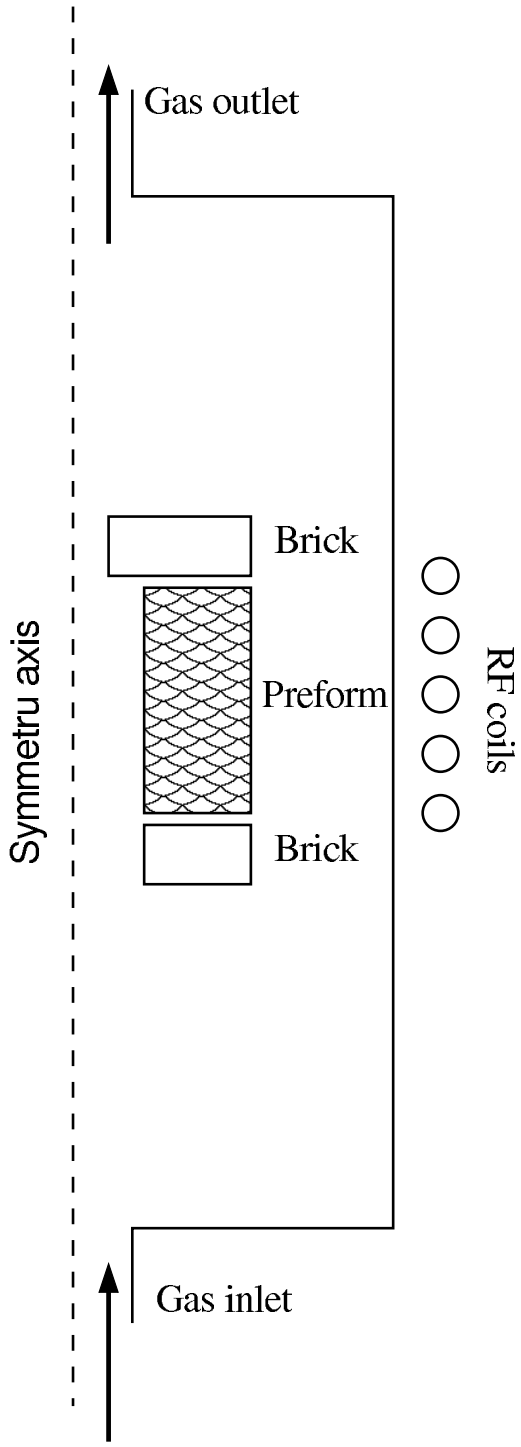
Gas outlet
Brick
Preform
Brick
RF coils
Symmetru axis
Gas inlet

Figure 1:

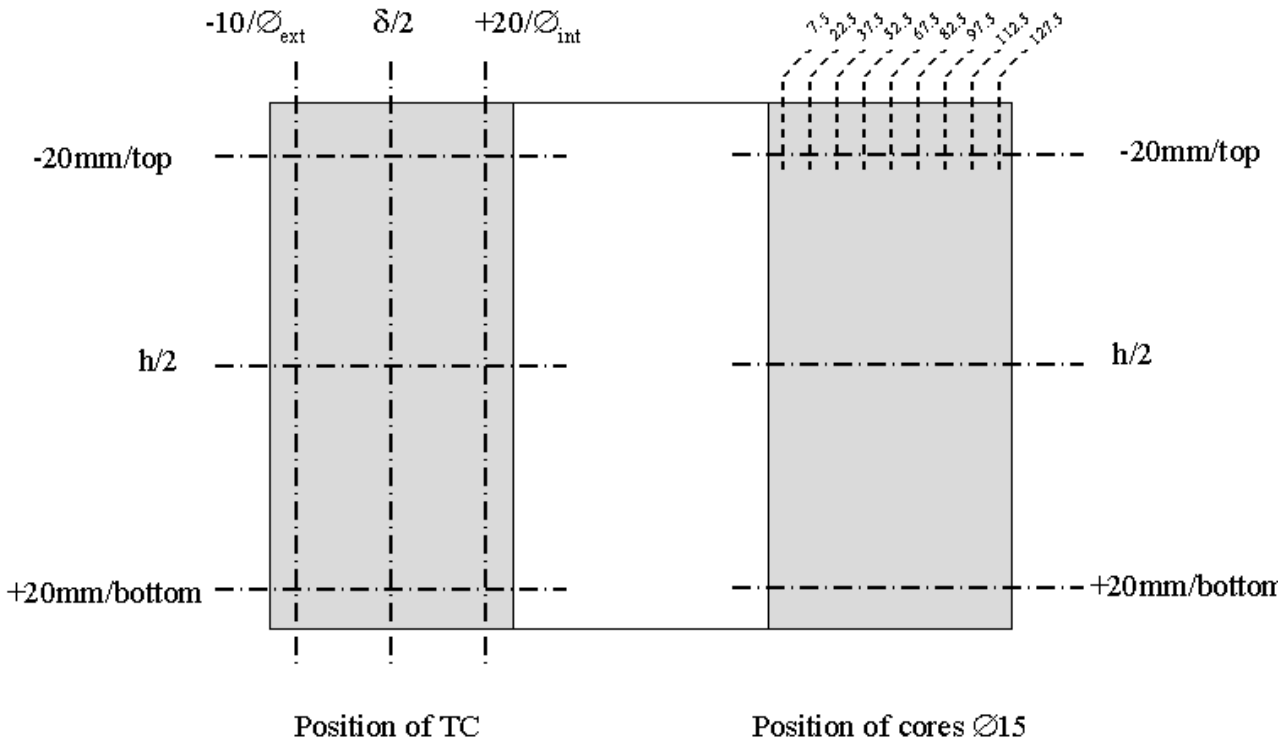
-10/∅ext
δ/2
+20/∅int
7.5
22.5
37.5
52.5
67.5
82.5
97.5
112.5
127.5
-20mm/top
h/2
+20mm/bottom
-20mm/top
h/2
+20mm/bottom
Position of TC
Position of cores ∅15

Figure 2:

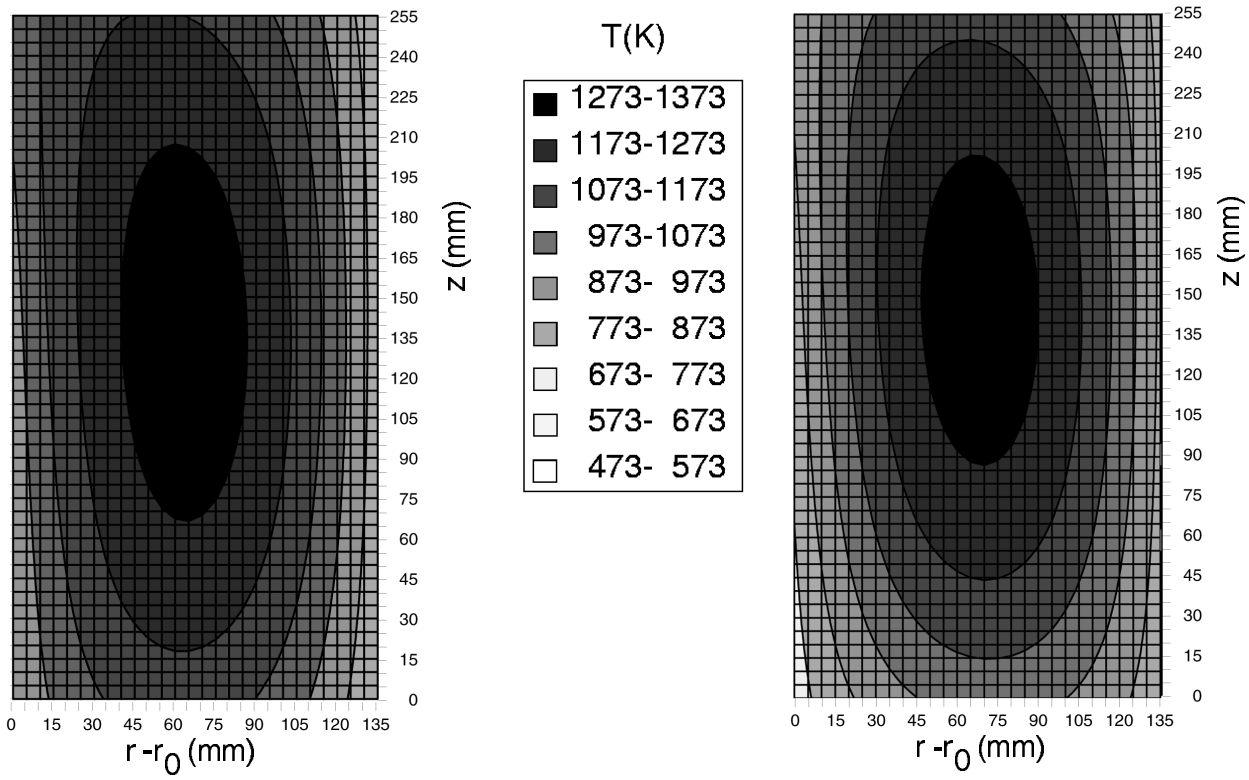
T(K)
1273-1373
1173-1273
1073-1173
973-1073
873- 973
773- 873
673- 773
573- 673
473- 573
z (mm)
r -r0 (mm)
0 15 30 45 60 75 90 105 120 135
0 15 30 45 60 75 90 105 120 135 150 165 180 195 210 225 240 255

Figure 3:

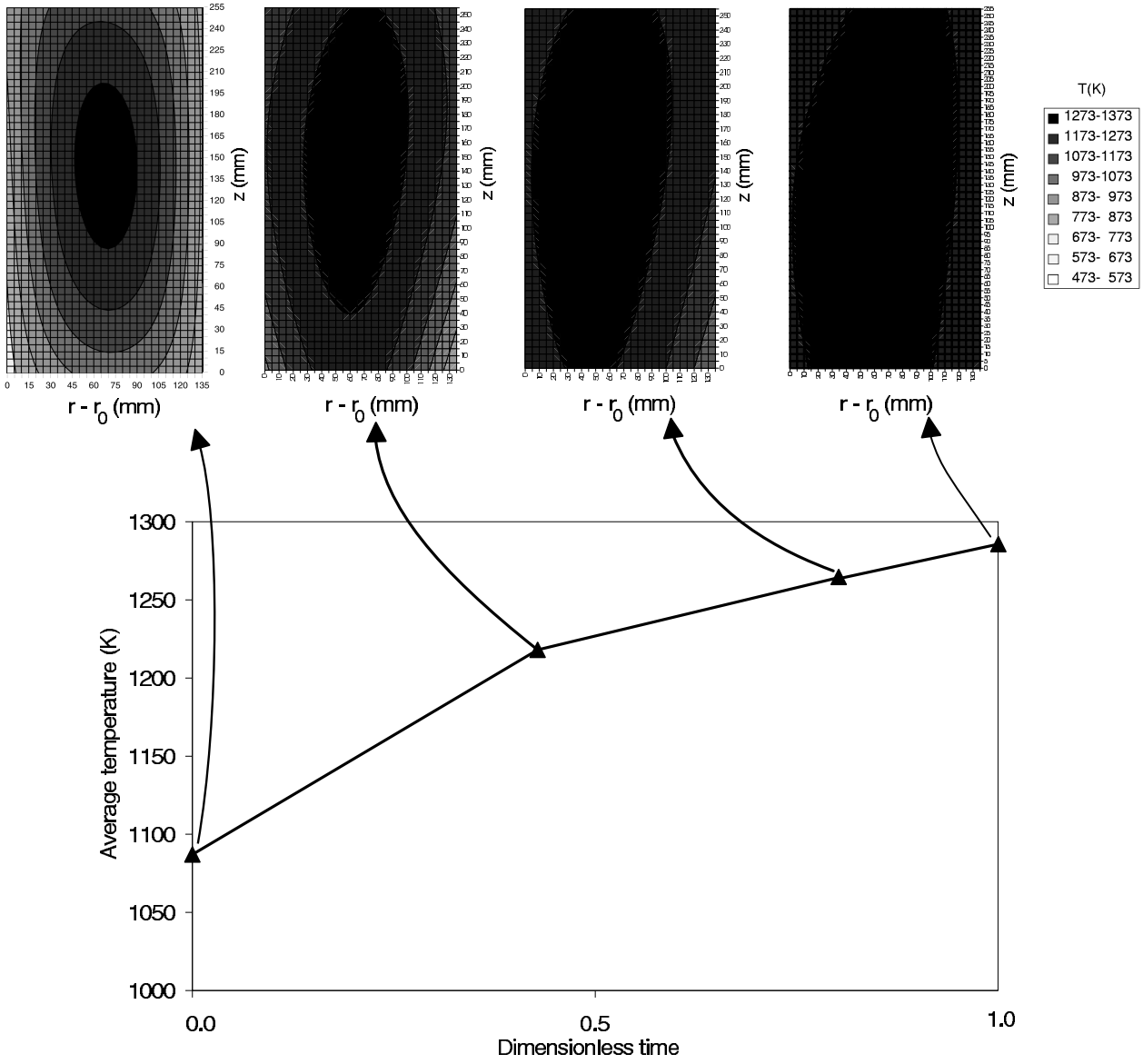
T(K)
1273-1373
1173-1273
1073-1173
973-1073
873- 973
773- 873
673- 773
573- 673
473- 573
z (mm)
r - r0 (mm)
Average temperature (K)
1300
1250
1200
1150
1100
1050
1000
0.0
0.5
1.0
Dimensionless time

Figure 4:

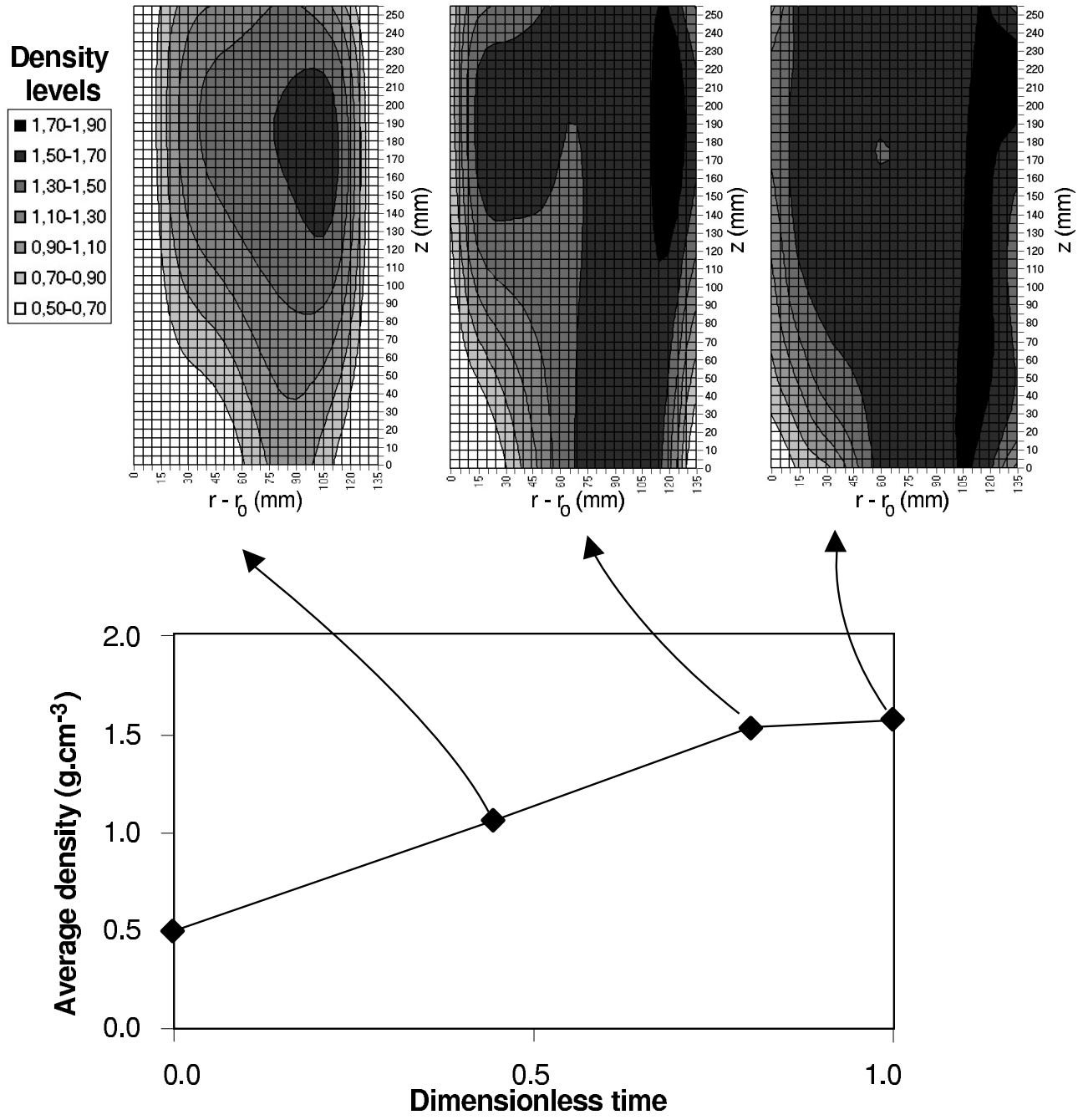
Density levels
1,70-1,90
1,50-1,70
1,30-1,50
1,10-1,30
0,90-1,10
0,70-0,90
0,50-0,70
z (mm)
r - r0 (mm)
Average density (g.cm-3)
Dimensionless time
0.0
0.5
1.0
1.5
2.0

Figure 5:

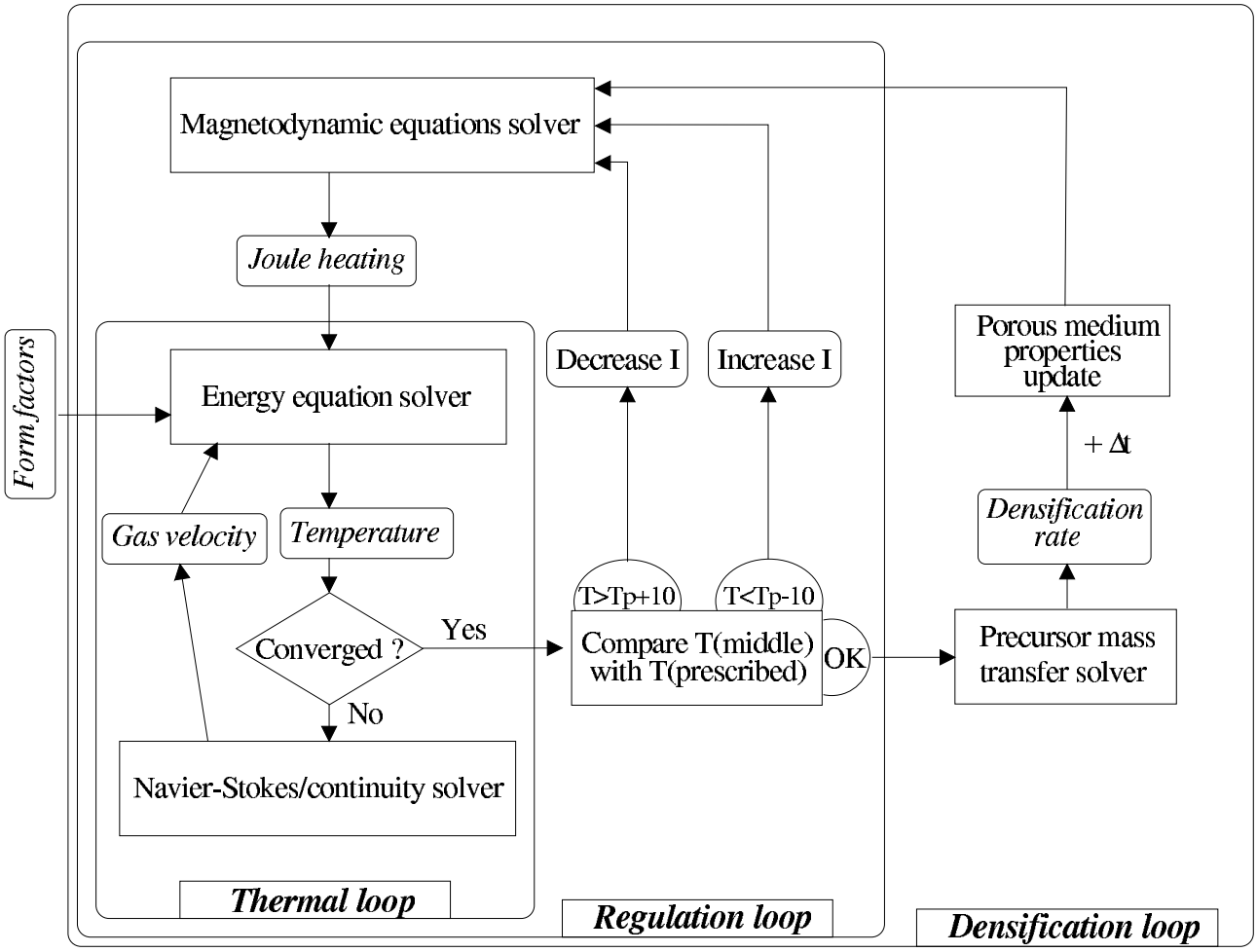
Magnetodynamic equations solver
Joule heating
Form factors
Energy equation solver
Gas velocity
Temperature
Converged ?
Yes
No
Navier-Stokes/continuity solver
Thermal loop
Decrease I
Increase I
T>Tp+10
T<Tp-10
Compare T(middle) with T(prescribed)
OK
Regulation loop
Porous medium properties update
+ Δt
Densification rate
Precursor mass transfer solver
Densification loop

Figure 6:

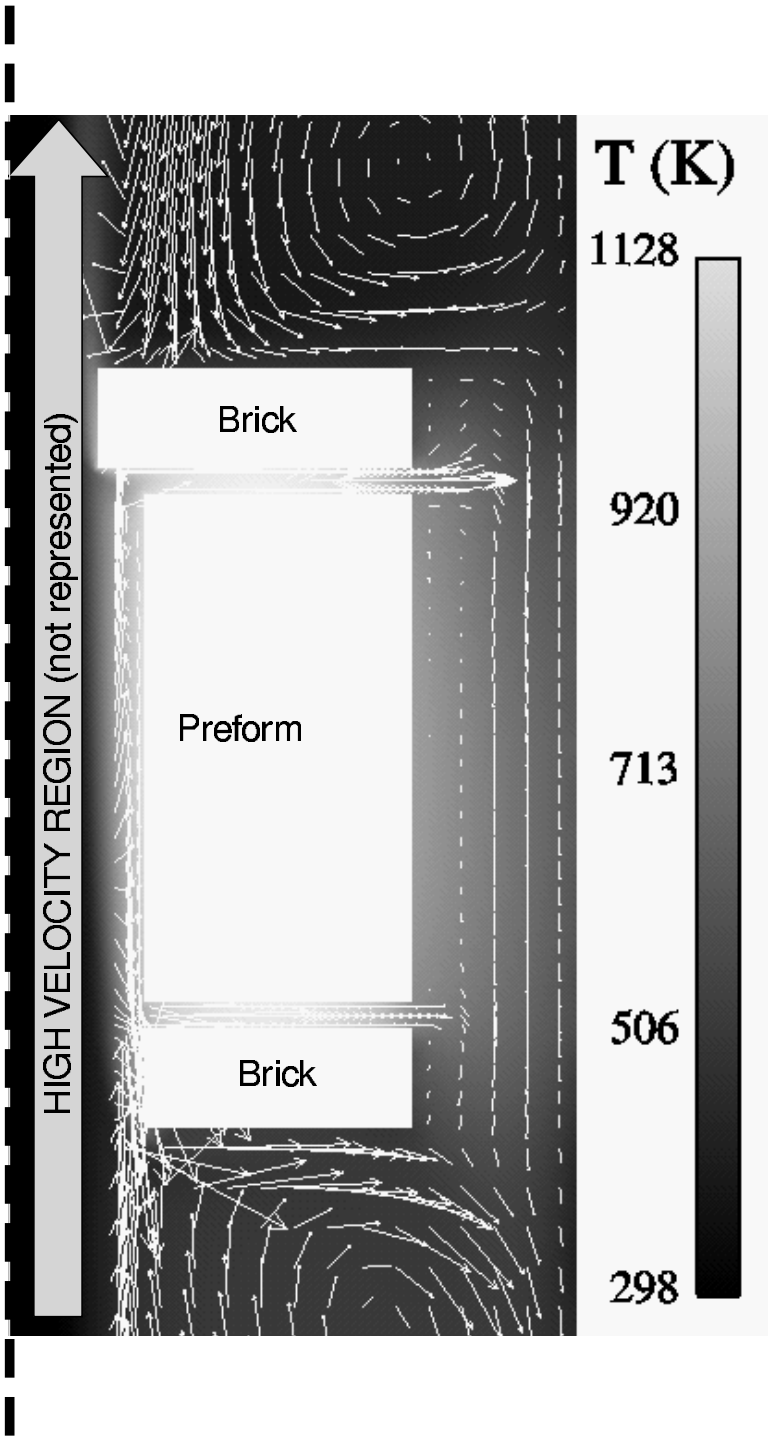
T (K)
1128
920
713
506
298
Brick
Preform
Brick
HIGH VELOCITY REGION (not represented)

Figure 7:

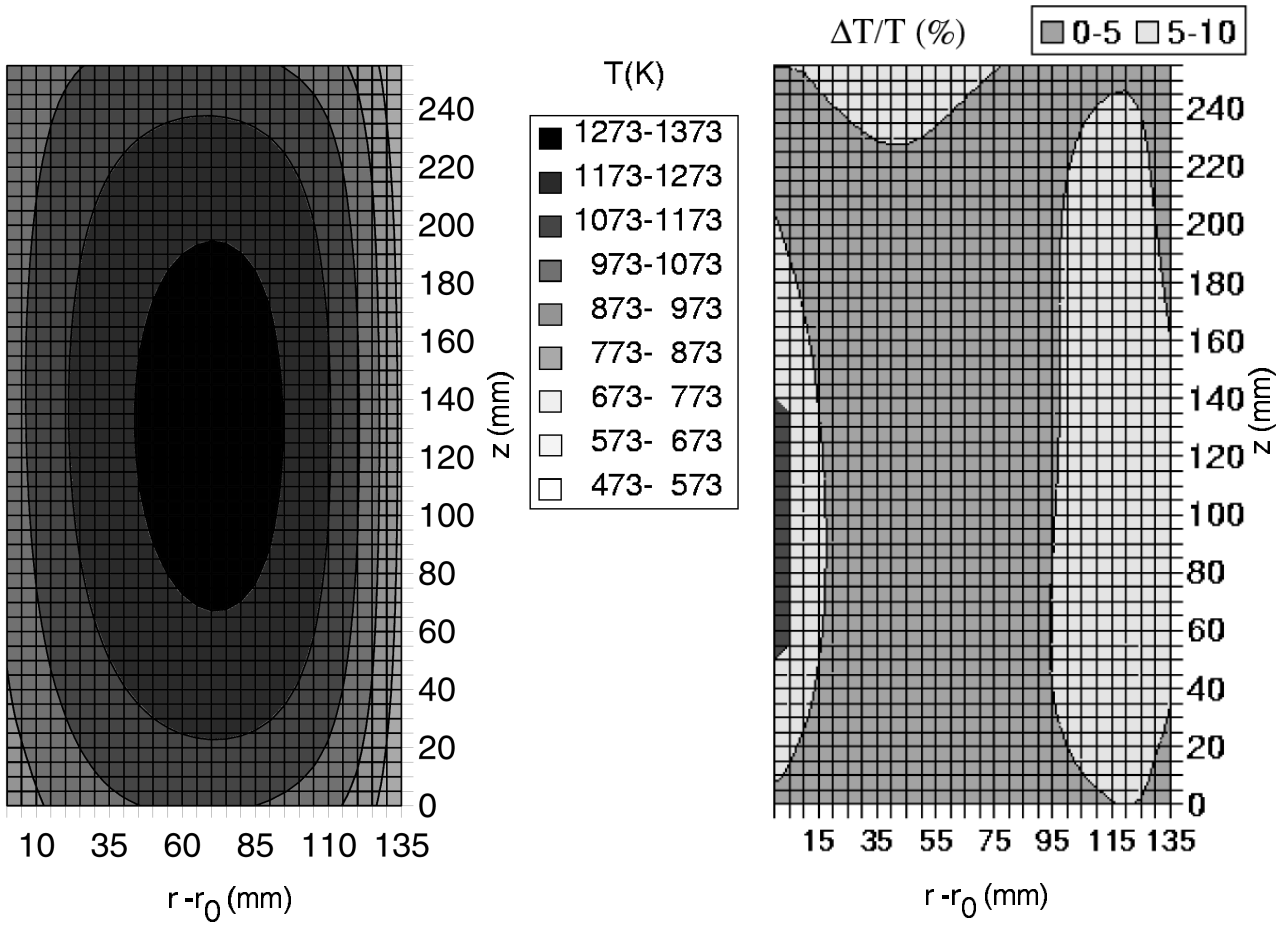
T(K)
1273-1373
1173-1273
1073-1173
973-1073
873- 973
773- 873
673- 773
573- 673
473- 573
z (mm)
240
220
200
180
160
140
120
100
80
60
40
20
0
10 35 60 85 110 135
r -r0 (mm)
ΔT/T (%)
0-5
5-10
15 35 55 75 95 115 135
r -r0 (mm)

Figure 8:

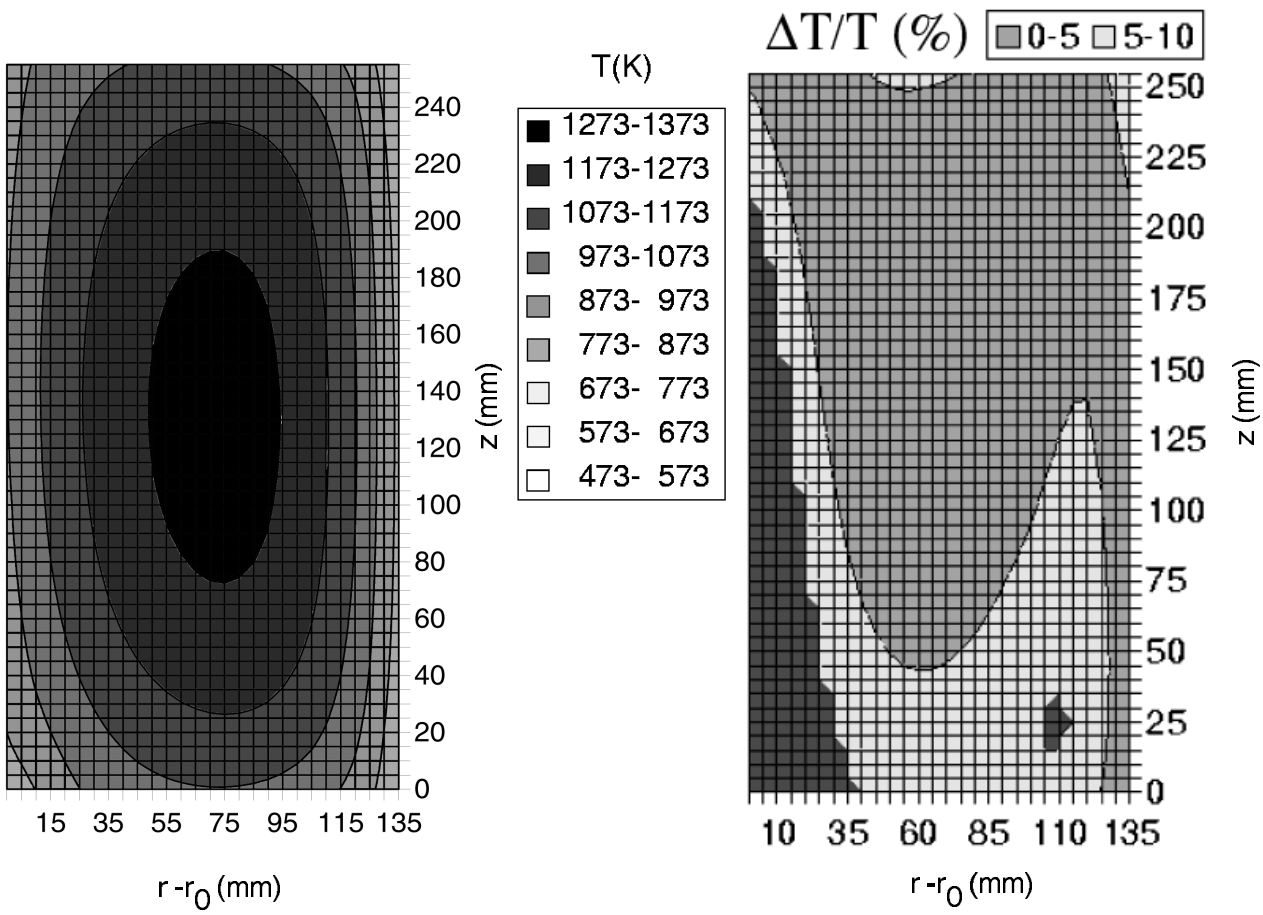
T(K)
1273-1373
1173-1273
1073-1173
973-1073
873- 973
773- 873
673- 773
573- 673
473- 573
z (mm)
240
220
200
180
160
140
120
100
80
60
40
20
0
15 35 55 75 95 115 135
r -r0 (mm)
ΔT/T (%)
0-5
5-10
250
225
200
175
150
125
100
75
50
25
0
z (mm)
10 35 60 85 110 135
r -r0 (mm)

Figure 9:

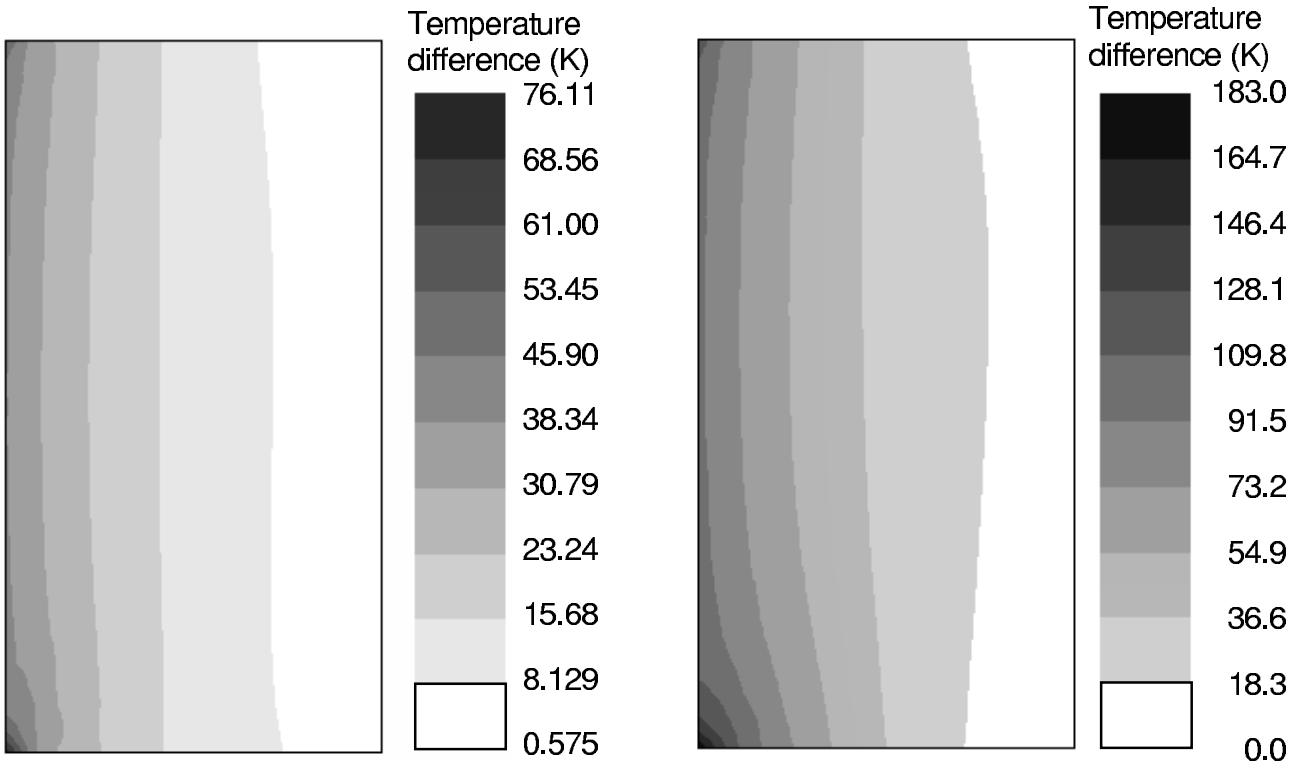
Temperature
difference (K)
76.11
68.56
61.00
53.45
45.90
38.34
30.79
23.24
15.68
8.129
0.575
Temperature
difference (K)
183.0
164.7
146.4
128.1
109.8
91.5
73.2
54.9
36.6
18.3
0.0

Figure 10:

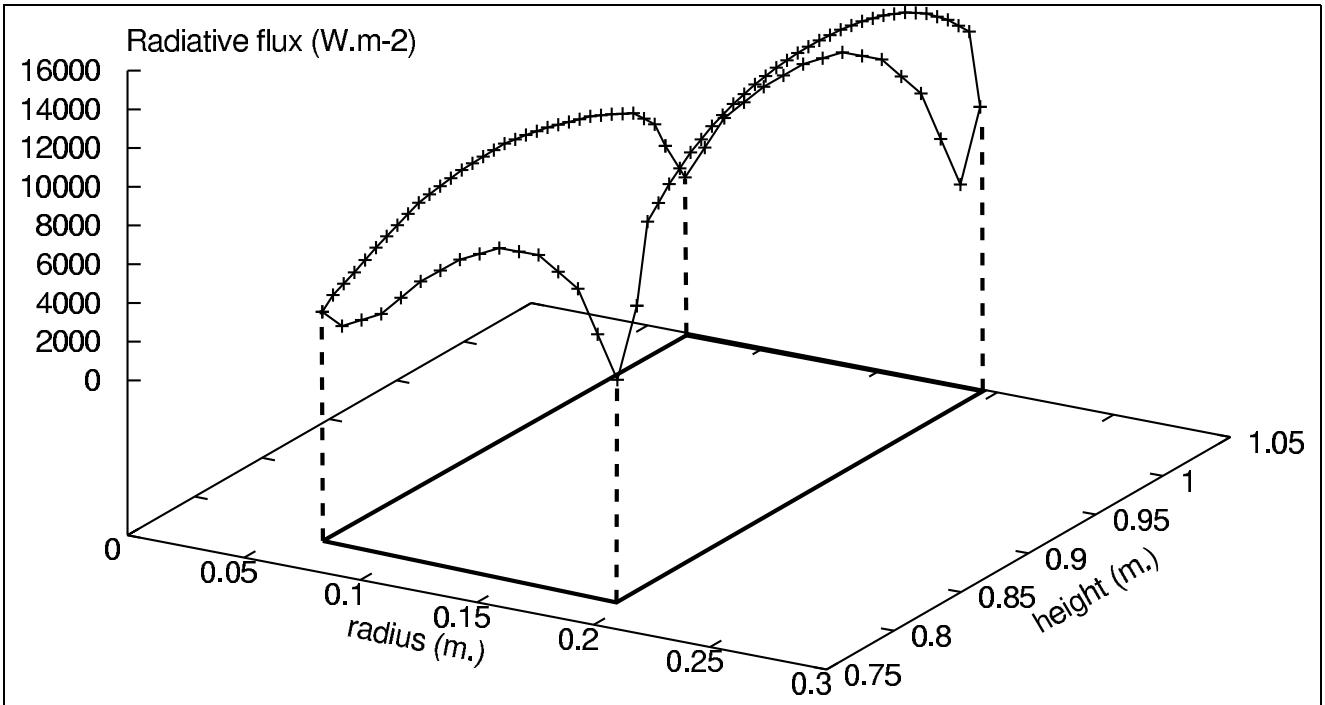
Radiative flux (W.m-2)
16000
14000
12000
10000
8000
6000
4000
2000
0
0
0.05
0.1
0.15
0.2
0.25
0.3
radius (m.)
0.75
0.8
0.85
0.9
0.95
1
1.05
height (m.)

a)

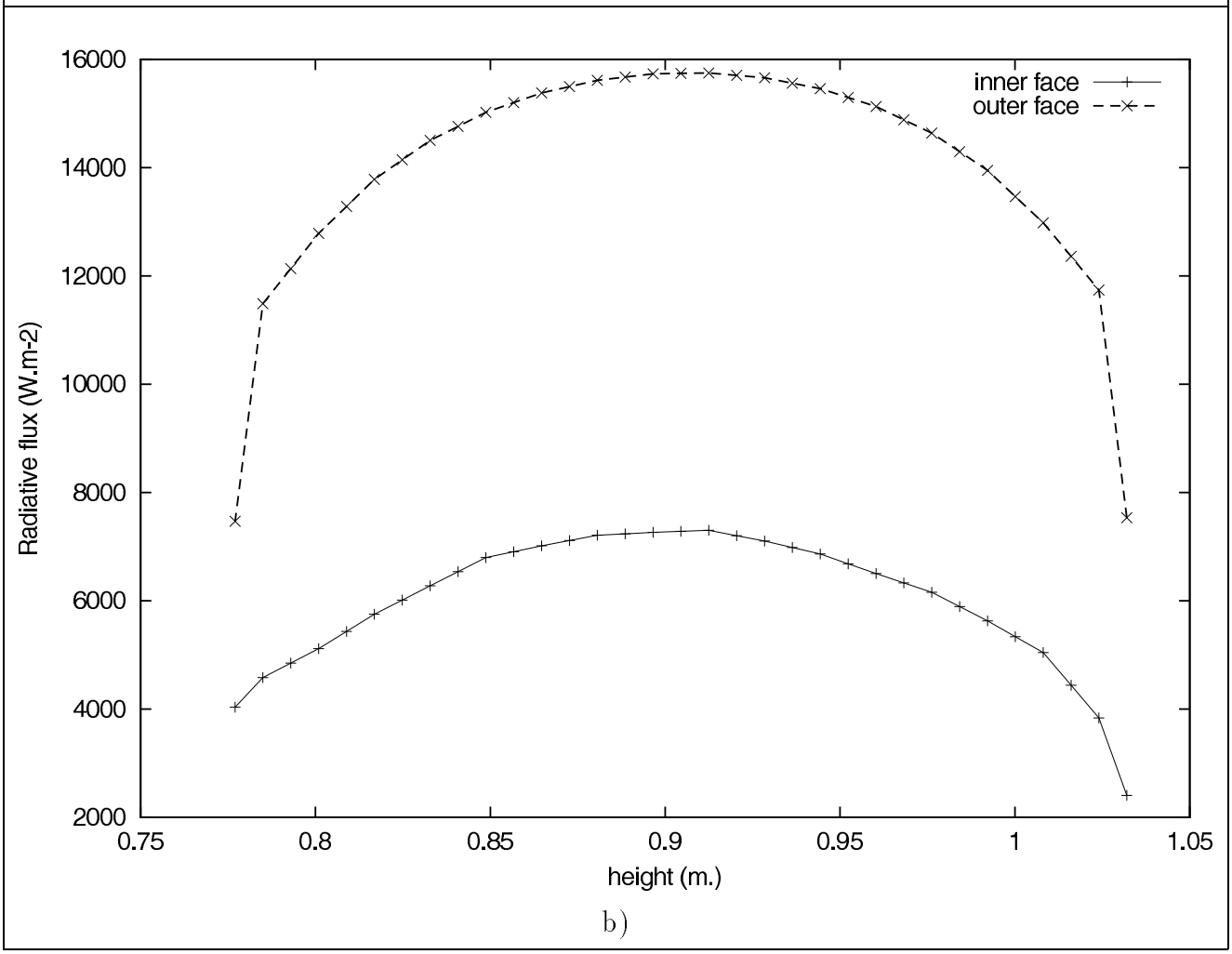
inner face
outer face
Radiative flux (W.m-2)
16000
14000
12000
10000
8000
6000
4000
2000
0.75
0.8
0.85
0.9
0.95
1
1.05
height (m.)

b)

Figure 11:

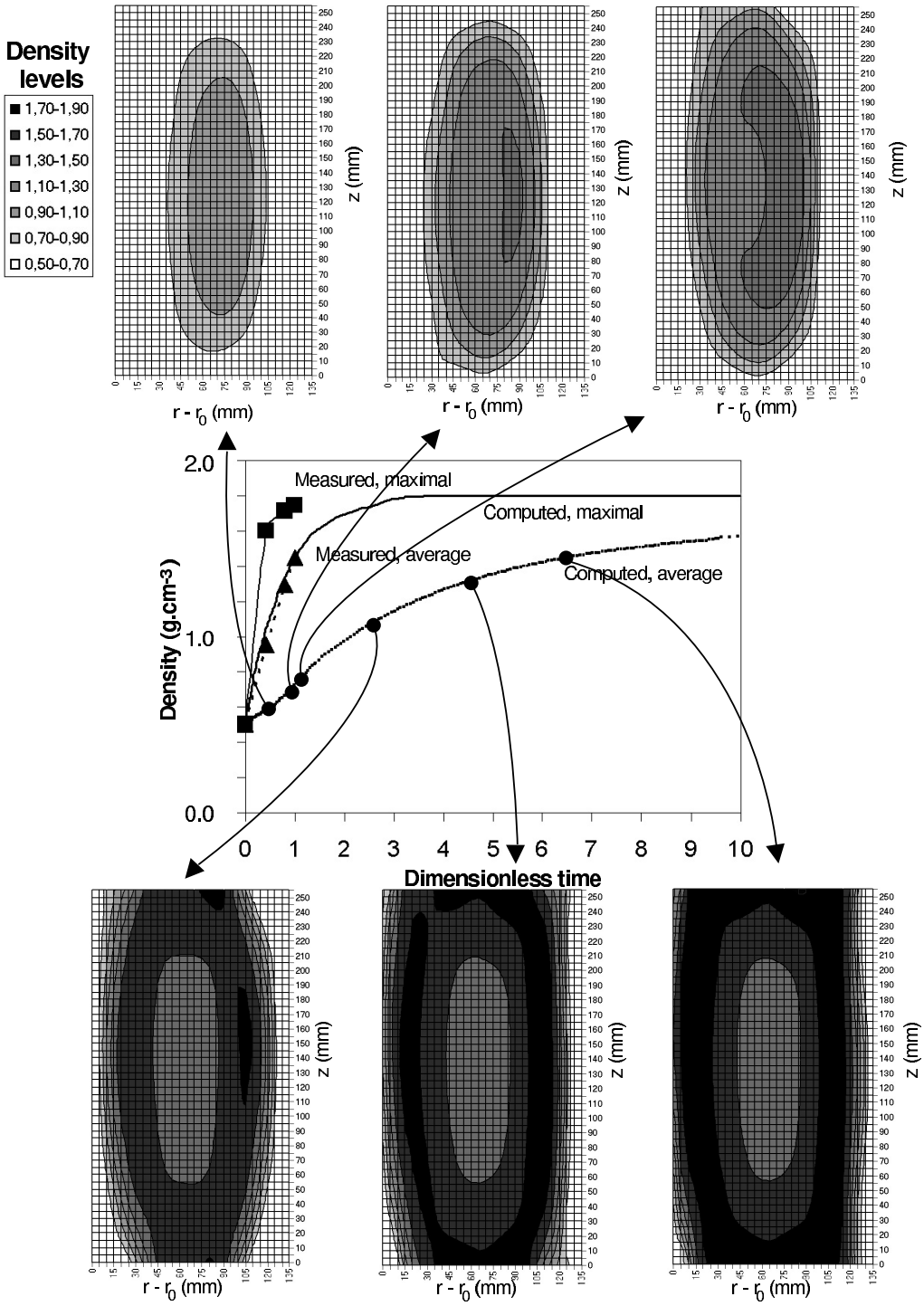
Density levels
1,70-1,90
1,50-1,70
1,30-1,50
1,10-1,30
0,90-1,10
0,70-0,90
0,50-0,70
r - r0 (mm)
z (mm)
Measured, maximal
Computed, maximal
Measured, average
Computed, average
Density (g.cm-3)
Dimensionless time
2.0
1.0
0.0
0 1 2 3 4 5 6 7 8 9 10

Figure 12:

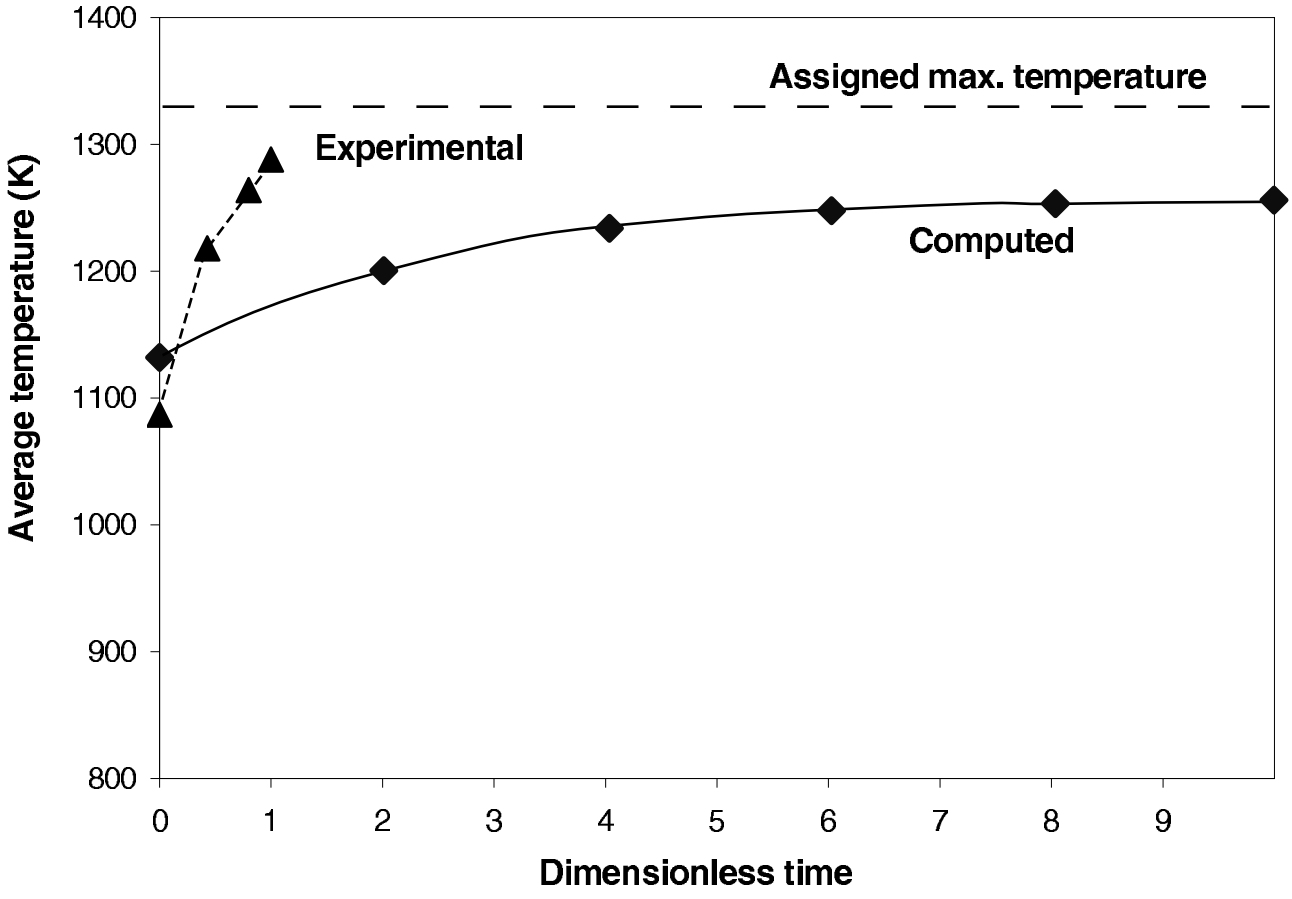
1400
1300
1200
1100
1000
900
800
Average temperature (K)
Assigned max. temperature
Experimental
Computed
0
1
2
3
4
5
6
7
8
9
Dimensionless time

Figure 13:

Table Captions.

- Table 1: Comparative presentation of previous modeling works on isobaric TG-CVI.
- Table 2: List of experimental parameter values.
- Table 3: List of provided parameter values for numerical simulations.
- Table 4: Dimensionless numbers for the gas flow.

Ref.	Heating	Cooling	Chemical system
1D models			
[30]	Linear T profile		$(CH_3)_2\,SiCl_2$
			$\rightarrow SiC + CH_4 + 2HCl$
[10]	Fixed inner temperature	Conv. and rad.	$3CO_2 + 3H_2 + 2AlCl_3$
			$\rightarrow Al_2O_3 + 6HCl + 3CO$
[22]	Constant power	Convective	$CH_3SiCl_3 \rightarrow SiC + 3HCl$
[23]	Constant power	Conv. and rad.	$CH_3SiCl_3 \rightarrow SiC + 3HCl$
[31]	Power = f(time)	Conv. and rad.	$CH_4 \rightarrow C + 2H_2$
[32]	Microwave (analytical)	Conv. and rad.	$CH_3SiCl_3 \rightarrow SiC + 3HCl$
[33]	Maxwell's equations	Conv. and rad.	$CH_3SiCl_3 \rightarrow SiC + 3HCl$
2D models			
[34]	Microwave (analytical)	Convective	$CH_3SiCl_3 \rightarrow SiC + 3HCl$
[14, 15]	Maxwell's equations	Conv. and rad.	$CH_4 \rightarrow C + 2H_2$

Table 1:

Parameter	Value
RF Heating	
Coil section diameter	$d_c = 16mm$
Assigned temperature	$T_c = 1323K$
Preform	
Inner diameter	$\oslash_{int} = 135 \ \ mm$
Outer diameter	$\oslash_{ext} = 405 \ \ mm$
Height	$H = 255mm$
Initial porosity	$\epsilon_0 = 0.72$
Minimal porosity	$\epsilon_f = 0.07$
Volumic mass-porosity relation	$d = 1.94 - 2\epsilon \ \ (g.cm^{-3})$
Gases	
Pressure	$P_{tot} = 2600 \ \ Pa$
Composition	Case 1 : N_2
	Case 2 : CH_4
Inlet flowrate	$Q = 10000 \ \ sccm$

Table 2:

Parameter	Value
	Reactor
Wall emissivity	$e = 0.85$
Thermal transfer coefficient	$h = 570 \;\; W.m^{-2}.K^{-1}$
Outer wall temperature	$T_{amb} = 298 \;\; K$
	Preform
Magnetic permeability	$\mu_r = 4\pi.10^{-7} \;\; H.m^{-1}$
Emissivity	$e = 0.8$
Electrical conductivity	$\sigma_{theta} = (1-\epsilon)\sigma_c$
	$\sigma_c = 25000 \;\; S.m^{-1}$
Thermal conductivity	$\lambda = [(1-\epsilon)^2 \lambda_c(T) + \epsilon^2 \lambda_g(T)]$
	$\lambda_{c,r} = 10.6 W.m^{-1}.K^{-1} \;\; @ \;\; 298K$
	$\lambda_{c,z} = 21.2 W.m^{-1}.K^{-1} \;\; @ \;\; 298K$
	$\partial\lambda_c/\partial T = 2.10^{-3} \;\; W.m^{-1}.K^{-2}$
	Gases
Composition	Case 1 : N_2
	Case 2 : 75% CH_4, 25% H_2
	Densification parameters
Internal surface	$\sigma_v = 3.10^5 (-0.2816 + 4.272\epsilon - 3.56\epsilon^2) \;\; m^{-1}$
Chemical deposition rate constant	$k = k_0 \; \exp\left(-\frac{E_a}{\mathcal{R}T}\right)$
	$k_0 = \frac{2.24 \; 10^{14}}{\sigma_{v,0}} \;\; m.s^{-1}$
	$E_a = 364 \;\; kJ.mol^{-1}$
Diffusivity	$D_{eff} = \left(D_b^{-1} + D_K^{-1}\right)^{-1} \;\; (m^2.s^{-1})$
Diffusivity (ordinary)	$D_{b,r}/D_{gas} = \epsilon^{3.43} \left(\frac{T}{298}\right)^{3/2}$
	$D_{b,z}/D_{gas} = \epsilon^{3.04} \left(\frac{T}{298}\right)^{3/2}$
Diffusivity (Knudsen)	$D_{K,r} = D_{K,0} \; \frac{\epsilon^2}{\sigma_v} \left(\frac{0.65}{\epsilon - 0.07}\right)^{1.005} \sqrt{\frac{T}{298}}$
	$D_{K,z} = D_{K,0} \; \frac{\epsilon^2}{\sigma_v} \left(\frac{0.65}{\epsilon - 0.07}\right)^{0.954} \sqrt{\frac{T}{298}}$
	$D_{K,0} = \frac{1}{3}\sqrt{\frac{8\mathcal{R} \times 298}{\pi M_{gas}}} \left(\frac{4\epsilon_0}{\sigma_{v,0}}\right)$
Deposit molar volume	$v_s = 5.45 \; 10^{-3} \;\; m^3.mol^{-1}$

Table 3:

Reactor zone	Local Re	Local $Ra.D/L$	Flow type [29]
Preform interior hole	5000	< 40000	transition ; forced
Outlet zone	5500	34000	transition ; forced
Void zones	< 1000	140000	laminar ; free

Table 4: